# Crustal anisotropy beneath Hudson Bay from ambient noise tomography: Evidence for post-orogenic lower-crustal flow?

Agnieszka Pawlak,[1] David W. Eaton,[1] Fiona Darbyshire,[2] Sergei Lebedev,[3] and Ian D. Bastow[4]

Received 29 November 2011; revised 13 June 2012; accepted 19 June 2012; published 1 August 2012.

[1] The crust underlying Hudson Bay, Canada records a long and complex tectonic history. In this study, we investigate this region using tomographic inversion based on continuous ambient noise recordings from 37 broadband seismograph stations that encircle Hudson Bay. The ambient noise data were processed to obtain group-velocity dispersion measurements from 10–35 s period, which were inverted using an algorithm that incorporates the effects of anisotropy. This work is among the first in which ambient noise data have been used to investigate azimuthal anisotropy. The inversion method uses smoothing and damping to regularize the solution; due to the significantly increased number of model parameters relative to the isotropic case, we performed a careful analysis for parameter selection to determine whether "leakage" occurs between isotropic and anisotropic model parameters. We observe a robust pattern of anisotropic fast directions in the mid-crust that are consistent with large-scale tectonic trends based on magnetic-anomaly patterns. In particular, a distinctive double-indentor shape for the Superior craton is clearly expressed in both data sets. This pattern breaks down deeper in the crust, suggesting that some degree of lithospheric decoupling in the lower crust, such as channel flow, occurred during orogenesis. Given regional evidence for vertically coherent deformation in the crust and underlying mantle, we interpret this pattern in the lower crust as a tectonic overprint that post-dates the main phase of Trans-Hudson deformation. At most levels in the crust, we observe a profound change in direction of anisotropic fast direction across an inferred suture beneath Hudson Bay.

**Citation:** Pawlak, A., D. W. Eaton, F. Darbyshire, S. Lebedev, and I. D. Bastow (2012), Crustal anisotropy beneath Hudson Bay from ambient noise tomography: Evidence for post-orogenic lower-crustal flow?, *J. Geophys. Res.*, *117*, B08301, doi:10.1029/2011JB009066.

## 1. Introduction

[2] Hudson Bay is a shallow inland sea that overlies the Paleozoic Hudson Bay basin, an intracratonic basin with stratigraphic record similar to the hydrocarbon-rich Williston, Illinois and Michigan basins (Figure 1). The Precambrian basement underlying the Hudson Bay basin was assembled by continental collisions culminating in the ca. 1.8 Ga Trans-Hudson Orogen (THO) [*Hoffman*, 1990; *Bickford et al.*, 1990; *Corrigan et al.*, 2005; *Eaton and Darbyshire*, 2010]. Teleseismic studies of mantle anisotropy have shown that upper-mantle anisotropic fabrics delineate many of the geologically inferred lithospheric sub-divisions to the north of Hudson Bay [e.g., *Bastow et al.*, 2011]. Similar analysis farther south beneath the Bay has not been possible to date, however, because of the absence of ocean-bottom seismometers to record body wave phases such as SKS. Therefore, whether the THO and/or earlier collisional events are preserved as fossil fabrics beneath the Bay remains unclear. Furthermore, loading by the Laurentide ice sheet, subsequent ongoing postglacial rebound and regional stresses induced by other sources may also manifest as measurable seismic anisotropic fabrics beneath the Bay. To address these issues, we investigate crustal anisotropy and seismic-velocity structure using ambient noise tomography (or seismic interferometry), using 21 months of continuous data acquired at 37 broadband seismograph stations located around the periphery of Hudson Bay (Figure 1a). This study builds on earlier work [*Pawlak et al.*, 2011] in which the isotropic seismic structure of the crust and upper mantle beneath Hudson Bay was imaged using the method of *Bensen et al.* [2007]. Although ambient noise tomography has been

[1]Department of Geoscience, University of Calgary, Calgary, Alberta, Canada.
[2]Centre de Recherche GEOTOP, Université du Québec à Montréal, Montréal, Québec, Canada.
[3]Geophysics Section, School of Cosmic Physics, Dublin Institute for Advanced Studies, Dublin, Ireland.
[4]School of Earth Sciences, University of Bristol, Bristol, UK.

Corresponding author: D. W. Eaton, Department of Geoscience, University of Calgary, 2500 University Dr. NW, Calgary, AB T2N 1N4, Canada. (eatond@ucalgary.ca)


0148-0227/12/2011JB009066

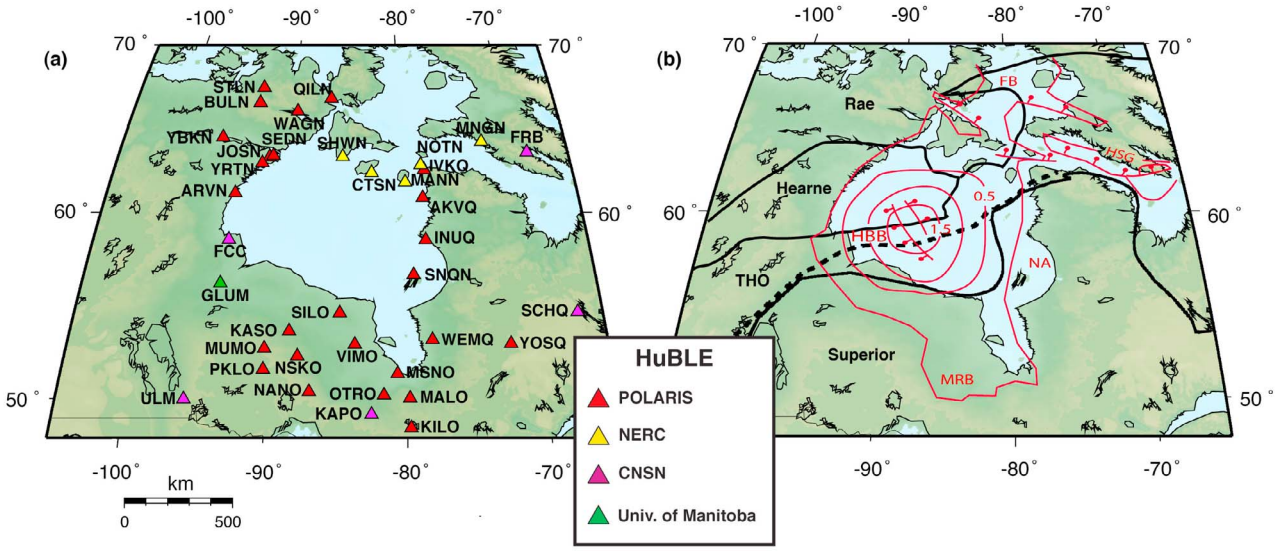


**Figure 1.** (a) Map of Hudson Bay showing all HuBLE stations used in this study. (b) Tectonic map of Hudson Bay. Solid black lines are approximate locations of tectonic boundaries and the dashed black line represents the suture zone. The red lines outline the location of the Hudson Bay basin, mapped faults and total sediment isopach contours in kilometers. Abbreviations are as follows: THO, Trans-Hudson orogen; FB, Foxe basin; HSG, Hudson Strait graben; HBB, Hudson Bay basin; NA, Nastapoka Arc; MRB, Moose River basin [after *Eaton and Darbyshire*, 2010].

widely used in recent years [e.g., *Shapiro et al.*, 2005; *Curtis et al.*, 2006; *Yao et al.*, 2006; *Yang et al.*, 2007; *Moschetti et al.*, 2007; *Lin et al.*, 2007, 2011], incorporating azimuthal anisotropy has only recently started to emerge [*Yao and van der Hilst*, 2009; *Fry et al.*, 2010; *Gallego et al.*, 2011; *Lin et al.*, 2011].

[3] Our investigation uses continuous recordings of ground motion from broadband seismograph stations deployed as part of the Hudson Bay Lithospheric Experiment (HuBLE), an international initiative with the broad aim of elucidating the lithospheric architecture beneath the Bay. To date, HuBLE data have been used to study various features and depth ranges, including receiver-function analysis of crustal structure [*Thompson et al.*, 2010] and mantle transition zone thickness [*Thompson et al.*, 2011], isotropic ambient noise tomography to investigate basin structure [*Pawlak et al.*, 2011], SKS-splitting investigation of upper-mantle anisotropy [*Bastow et al.*, 2011] and surface-wave studies of the lithospheric keel [*Darbyshire and Eaton*, 2010].

[4] After providing an overview of the isotropic ambient noise processing procedure, we introduce an anisotropic tomography method that has been previously applied for the inversion of teleseismic surface-wave measurements and for array tomography using earthquake signals [*Lebedev and van der Hilst*, 2008; *Deschamps et al.*, 2008; *Darbyshire and Lebedev*, 2009]. Following this, we present the results of anisotropic tomography together with a comprehensive analysis of parameter selection for the inversion process. Finally, we interpret the inferred anisotropic fabric by comparing our results with stress data, plate-motion directions and regional total-field magnetic anomaly data. Our results indicate that contrasting mid-crustal anisotropic fabrics are juxtaposed across the principal lithospheric suture within the THO, suggesting that these fabrics were formed prior to terminal collision.

## 2. Tectonic Setting

[5] Hudson Bay is a shallow (~100 m deep) epeiric sea, approximately 1000 km in diameter that formed by marine inundation of the continental interior following Laurentide ice sheet deglaciation [*Lee*, 1968]. The Bay is located near the center of the North American continent (Figure 1b), and the underlying crust preserves a record of Paleoproterozoic collisional assembly of Laurentia and subsequent formation of the Hudson Bay basin, with minor intraplate deformation coeval with the Cretaceous opening of Baffin Bay [*Burden and Langille*, 1990; *Eaton and Darbyshire*, 2010]. With an area of ~833,000 km$^2$ and a maximum preserved stratigraphic thickness of ~2 km, the Hudson Bay basin is slightly more extensive but shallower than comparable intracratonic basins in North America (Michigan, Williston, Illinois).

[6] Beneath the Hudson Bay basin, the Precambrian basement is comprised mainly of the ca. 1.91–1.81 Ga THO and bounding Archean cratons (Figure 1b), including the Superior craton to the south and east and the Churchill craton (Hearne and Rae Domains) to the north and west. Similar in spatial and temporal scales to the modern Himalayan-Karakoram-Tibetan orogeny [*St.-Onge et al.*, 2006], the THO formed as a result of collision between the Superior and Churchill protocontinents [*Eaton and Darbyshire*, 2010]. Paleomagnetic evidence suggests that these two large Archean cratons were once separated by a Pacific-scale ocean (Manikewan Ocean) [*Symons and Harris*, 2005], the closure of which is manifested by a suture that extends across Hudson Bay (Figure 1b) [*Eaton and Darbyshire*, 2010]. Continental arc formation due to pre-collision convergence

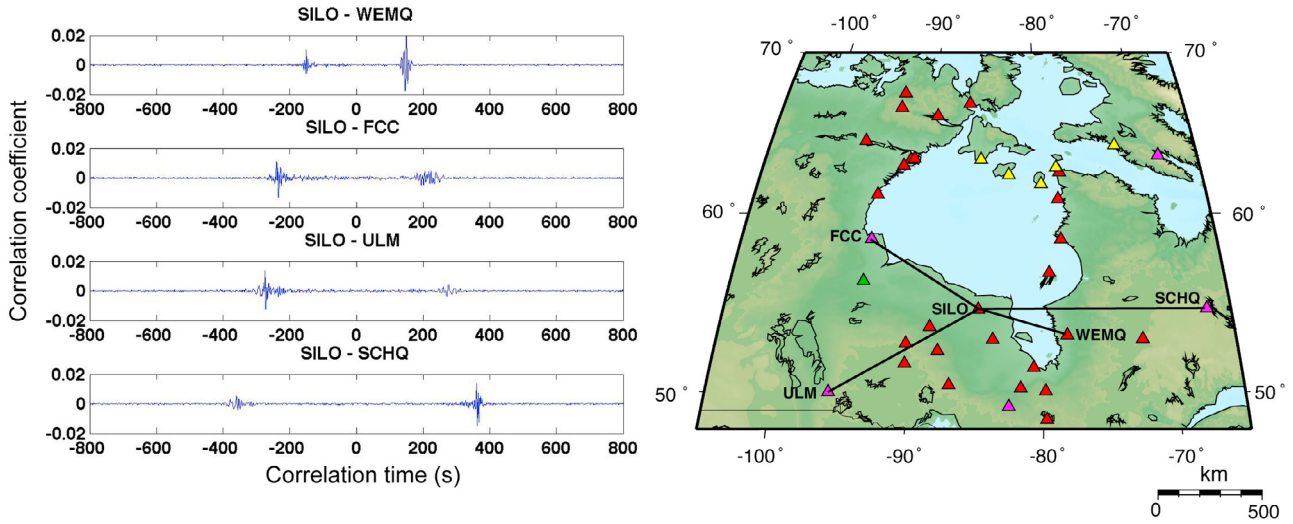


**Figure 2.** (left) Examples of four cross-correlations illustrating asymmetry of correlograms with respect to signal-to-noise ratio (SNR), typical of this data set. (right) Corresponding paths are shown. Station order represents direction of wave propagation, i.e., for SILO – WEMQ, the negative lag represents wave propagation from SILO to WEMQ and the positive lag represents wave propagation from WEMQ to SILO.

and ocean-basin closure is represented by the giant Wathaman-Chipewyan batholith. Where exposed adjacent to Hudson Bay, the THO contains both juvenile supracrustal domains as well as blocks of pre 1.91 Ga crust, such as the Archean Sask craton [*Hajnal et al.*, 2005]. The lithospheric mantle beneath Hudson Bay has high shear velocity and is estimated to be at least 200 km in thickness, characteristics that are typical of Archean mantle keels [*Darbyshire and Eaton*, 2010]. It has been suggested that the broad, shallow character of the Hudson Bay basin relative to other intracratonic basins may be due to the relatively stiff flexural rigidity of the lithospheric keel at the time of basin formation [*Eaton and Darbyshire*, 2010].

## 3. Data and Processing Methods

[7] The data used for the present study were recorded at a sampling rate of 40 Hz over 21 months, from September 2006 to May 2008. Initial data processing procedures follow the method of *Bensen et al.* [2007]. First, the continuous vertical-component recordings were cut into individual one-day records and resampled to 1 Hz. Next, daily trends, means and instrument-response functions were removed. Earthquake signals and instrument irregularities that could obstruct the signals of interest were suppressed using a one-bit time-normalization procedure. Finally, spectral whitening and band-pass filtering between 0.005 Hz and 0.3 Hz (200 s to 3.33 s period) were applied. Initial data processing procedures are detailed further by *Pawlak et al.* [2011].

[8] After completion of initial processing, correlograms were computed for all possible station pairs using available daily records. For each station pair, stacking of the daily cross-correlated signals yields a band-limited estimate of the inter-station Green's function [*Bensen et al.*, 2007] containing both causal and acausal components (Figure 2). For the vertical-component data in this study, emergent signals are dominated by fundamental-mode Rayleigh waves with periods of ~10–30 s that originate at coastal areas around North America [*Pawlak et al.*, 2011]. Based on visual inspection of the stacked correlograms, of 666 available station pairs, 591 were found to be usable.

[9] Figure 2 shows a representative example of a stacked correlogram showing both causal and acausal components of the Green's function. This example exhibits a pronounced asymmetry in which one half of the Green's function is characterized by a conspicuously higher signal-to-noise ratio (SNR) than the other half. This asymmetry originates from an inferred non-uniform distribution of coastal source locations [*Pawlak et al.*, 2011]. Since this asymmetry characterizes most of our data, instead of the typical approach [e.g., *Bensen et al.*, 2007] of averaging both sides to obtain a one-sided empirical Green's function (EGF), here we select for further processing the side of the correlogram having higher SNR [*Pawlak et al.*, 2011]. Choosing the higher SNR yields better dispersion ridges in our data compared with the averaging method [*Pawlak et al.*, 2011]. We remark that determination of group velocity in this manner is compatible with anisotropic models for the crust that are considered below, since all models exhibit identical wave speed in opposite directions (i.e., periodicity of $\pi$ radians).

[10] The EGFs derived in this fashion were then used for estimating group velocities based on time-frequency analysis (Figure 3). In our implementation of this procedure, the time-frequency plot is constructed for a given central frequency by applying a narrow-band filter to the EGF and then computing the amplitude envelope [*Pawlak et al.*, 2011]. Group velocity is obtained as a function of period by tracking the maximum amplitude such that a continuous dispersion curve is obtained. The shape of the dispersion curve is strongly influenced by the thickness of the crust and shows a clear transition from low velocity in the crust to high velocity in the underlying mantle (Figure 3). The group-velocity estimates are used as the basis for tomographic inversions that solve for period-specific models of

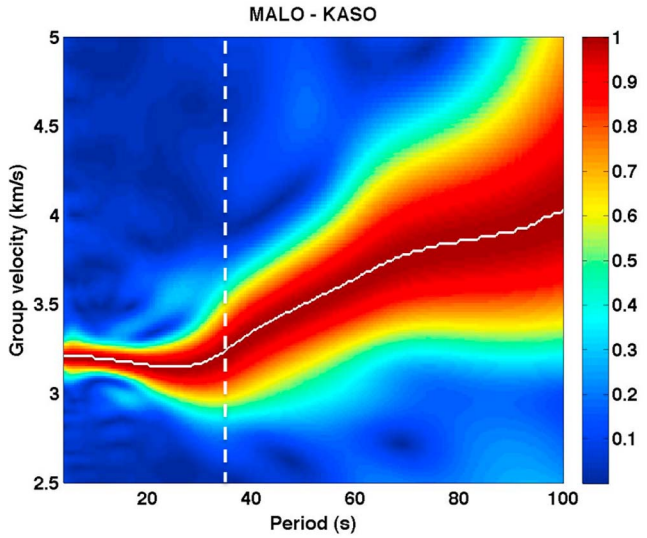


**Figure 3.** Example time-frequency plot and dispersion analysis. The color scale shows the amplitude envelope, normalized for each period value. The solid white line represents the group-velocity dispersion curve used as input for the inversion procedure. The dashed white line shows an approximate boundary between periods at which group-velocities are sensitive primarily to the crust (left of the line) and primarily to the mantle (right of the line).

the fundamental-mode Rayleigh-wave group velocity and azimuthal anisotropy beneath Hudson Bay.

## 4. Inversion

[11] We use a tomographic inversion scheme that has been used in analysis of interstation phase-velocity measurements made with teleseismic surface waves [*Deschamps et al.*, 2008; *Darbyshire and Lebedev*, 2009; *Endrun et al.*, 2011]. We remark that, within the usable bandwidth of the data (generally ~10–35 s period for most EGFs in our data set), the raypath coverage afforded by ambient noise measurements (Figure 4a) is well suited to anisotropic analysis because it contains nearly the full range of two-station azimuths possible for any given station distribution. The first step is to subtract the mean value of group velocity from all measurements, at each period. For the *i*th station pair, this yields a residual inter-station average group velocity, $\delta U_i(\omega) \pm \Delta U_i(\omega)$, where $\Delta U_i$ is the measurement uncertainty (estimated here to be 0.1 km/s). Working at Earth's surface within a spherical coordinate system defined by $\theta$, $\phi$ (Figure 4b), $\delta U_i(\omega)$ can be expressed in terms of the group-velocity model perturbations $\delta U(\omega, \theta, \phi)$ as

$$\int_{\theta}\int_{\phi} K_i(\theta,\phi)\delta U(\omega,\theta,\phi)d\phi\, d\theta = \delta U_i(\omega), \tag{1}$$

where $\omega$ is angular frequency and $K_i$ defines a sensitivity function for the *i*th station pair. Following *Darbyshire and Lebedev* [2009], the sensitivity function is defined here by rays along inter-station great circle paths (finite-width rays can also be easily accommodated within this formalism). To account for the effects of weak Rayleigh-wave anisotropy, the group-velocity perturbations $\delta U(\omega, \theta, \phi)$ are parameterized using 5 unknowns [*Smith and Dahlen*, 1973]:

$$\begin{aligned}\delta U(\omega) = \delta U_{iso}(\omega) + A_1(\omega)\cos(2\Psi) + A_2\sin(2\Psi)\\ + A_3(\omega)\cos(4\Psi) + A_4(\omega)\sin(4\Psi),\end{aligned} \tag{2}$$

where $\delta U_{iso}$ is the isotropic group-velocity perturbation and $\Psi$ denotes the wave-propagation azimuth with respect to geographic north. Terms that depend on $2\Psi$ and $4\Psi$ in equation (2) account for azimuthal variations of group velocity that exhibit a periodicity of $\pi$ and $\pi/2$ radians, respectively.

[12] The 5 model parameters in equation (2) are computed on a coarse (200 km) triangular model grid (Figure 4b), where the knot-point locations are determined using the method of *Wang and Dahlen* [1995]. The integration used to construct equation (1) is performed using a dense (40 km) integration grid of knot points (Figure 4b). For every

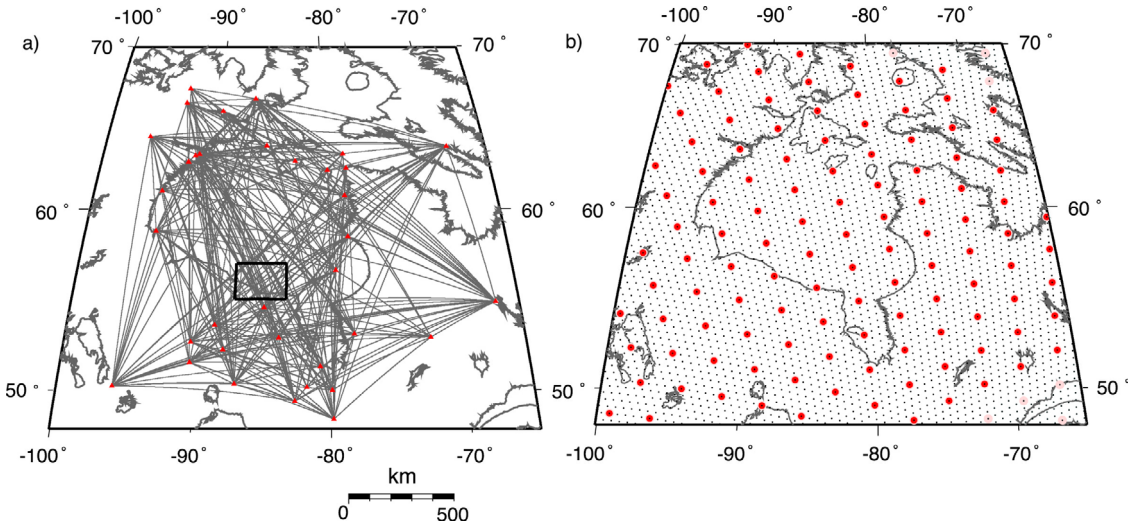


**Figure 4.** (a) Path density diagram. Black box shows paths used in Figure 6. (b) Map showing model-grid (red circles) and integration-grid (black circles) knots.

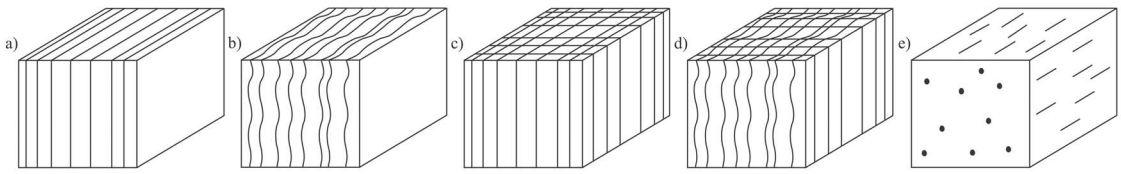


**Figure 5.** Schematic representation of (a) vertical cracks; (b) metamorphic foliation; (c) mutually perpendicular vertical cracks; (d) metamorphic foliation with perpendicular vertical cracks; (e) lattice preferred orientation (LPO) of orthorhombic minerals.

integration knot, a hexagonal region centered on the knot point is considered, whose vertices are made up of the six nearest points. The integration weight is first calculated at each of the integration-grid knot points located within one inter-knot distance from the interstation great circle path and is proportional to the area of the hexagon around it. The weights $K$ for the model parameters at model grid knots are then computed as integrals over the neighboring integration-grid knots [*Lebedev and van der Hilst*, 2008].

[13] At each of the 6 selected periods (10, 15, 20, 25, 30, 35 s), a sparse system of linear equations was constructed using equations (1) and (2) for all available paths. The resulting system was then solved iteratively using LSQR [*Paige and Saunders*, 1982], with smoothing and gradient damping. Gradient damping is a type of regularization that penalizes the difference between anomalies at each pair of neighboring knot points. This is similar to damping the first spatial derivative of the distributions of seismic velocity and anisotropy. Model smoothing is based on the difference between the anomaly at a grid knot and the average over anomalies at this and all neighboring knots. This second kind of smoothing is similar to damping the second spatial derivatives.The smoothing and damping parameters are assigned independently for $\delta U_{iso}$ and the 4 anisotropic parameters, and their selection plays a critical role in the inversion. Testing and selection of the smoothing and damping parameters is described in detail in Appendix A.

[14] At this stage, we consider a number of simple scenarios to illustrate how 2Ψ and 4Ψ symmetry might relate to fracture systems and/or alignment of intrinsically anisotropic minerals in the continental crust. In evaluating these scenarios, we invoke Neumann's principle [*Winterstein*, 1990] to relate the symmetry properties of the medium to the corresponding symmetry of wave propagation in the medium. For example, a single set of vertical cracks or sheet-like intrusions (dykes) in an otherwise isotropic medium would give rise to an azimuthally anisotropic system that exhibits 2Ψ symmetry for horizontally propagating Rayleigh waves (Figure 5a). In this scenario, the plane of the cracks (dykes) is expected to be perpendicular to the minimum principal stress direction at the time of formation [*Crampin*, 1994]. *Crampin* [1987] has proposed a more general crustal model, referred to as extensive-dilatancy anisotropy, in which pore spaces deform in response to the ambient stress field in a manner that would exhibit the same symmetry behavior as this crack model. Alternatively, azimuthal anisotropy could result from a pervasive metamorphic fabric that produces a strong crystallographic preferred orientation (Figure 5b). This could occur for a single dominant, near-vertical foliation or near-horizontal lineation fabric that is expressed by strongly anisotropic minerals such as mica and amphibole [*Meltzer and Christensen*, 2001; *Mahan*, 2006]. Such rock fabrics are commonly observed in metamorphic terranes around Hudson Bay [*Lee*, 1968]. Moreover, laboratory studies of metamorphic rocks [*Brocher and Christensen*, 1990] and seismological observations of the continental crust [e.g., *Paulssen*, 2004; *Shapiro et al.*, 2004; *Moschetti et al.*, 2010; *Endrun et al.*, 2011; *Lin et al.*, 2011] have documented strong azimuthal and radial anisotropy in various tectonic settings.

[15] Similarly, a 90° periodicity in Rayleigh-wave group velocity implied by the 4Ψ symmetry could be produced by several common geologic scenarios. For example, two sets of mutually perpendicular vertical cracks (Figure 5c) would yield an orthorhombic anisotropic system [*Winterstein*, 1992] with 4Ψ symmetry. Perpendicular crack systems (or pairsets as termed by *Gay* [1973]) are commonly observed in crustal rocks. The pairsets are believed to have formed simultaneously due to vertical motion or vertically directed forces and are perpetuated through cycles of regional metamorphism [*Gay*, 1973]. A second possibility is a single set of vertical cracks within a transversely isotropic medium, such as crustal rocks with a strong crystallographic preferred orientation as described above (Figure 5d). Finally, a well-developed crystallographic preferred orientation caused by alignment of minerals that exhibit orthorhombic seismic anisotropy (Figure 5e) [*Barruol and Mainprice*, 1993; *Mandeville*, 2010], could give rise to 4Ψ symmetry. Such a scenario is commonly invoked to explain seismic anisotropy of the upper mantle due to crystallographic preferred orientation of olivine [*Zhang and Karato*, 1995; *Smith et al.*, 2004].

[16] Given the possible geologic scenarios commonly seen in the crust, our data set was analyzed to evaluate the relative contribution of 2Ψ and/or 4Ψ variations. A selection of data taken from an area of dense path coverage (this region is shown by the black box in Figure 4a) at the 20 s period is shown in Figure 6. The 20 s period is used here because it has the most data and densest path coverage. An L1 norm was used to find a best fit to our data points, as an L1 norm is robust to outliers unlike the L2 norm [*Drulea et al.*, 2010]. The solid black line represents the L1 norm best fit for 2Ψ variations and the dashed black line is the L1 norm best fit for 4Ψ variation. The red line is the L1 best fit to the data, and the sum of the 2Ψ and 4Ψ variations. This data set (Figure 6), which is representative of data where path coverage exhibits a good azimuthal distribution (Figure 4a), shows a clear dominance of the 2Ψ signal; henceforth, for simplicity, we limit our interpretations to the 2Ψ case. However, this does not necessarily mean that 4Ψ anisotropy does not exist in the crust here, but that it perhaps simply may not be resolved by our data. Invoking Neumann's principle, we omit from further consideration models

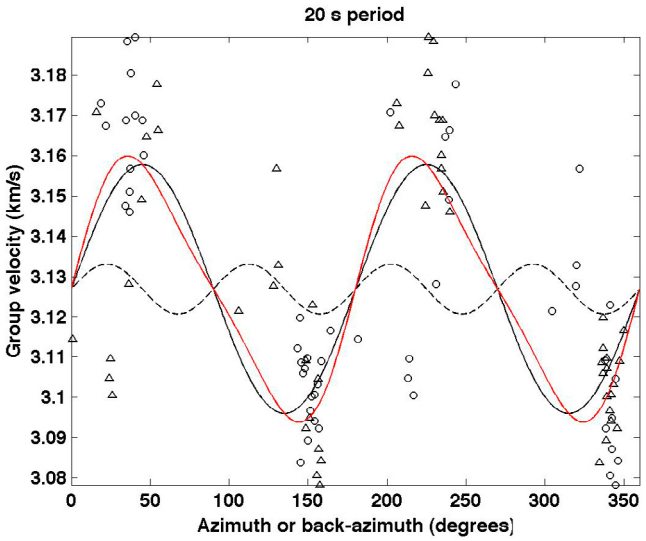


**Figure 6.** A selection of data taken from an area of dense path coverage at 20 s period path locations are shown with the black box in Figure 4a. Solid black line represents the L1 norm best fit for 2Ψ variations; the dashed black line is the L1 norm best fit for 4Ψ variations. The red line is the L1 best fit to the data, and the sum of the 2Ψ and 4Ψ variations.

defined by a 4Ψ symmetry system (i.e., Figures 5c–5e). We envision that there could be a "pseudo 2Ψ" model, similar to scenarios seen in Figures 5c and 5d, where one of the fracture or foliation systems is dominant over the other.

## 5. Resolution Testing

[17] In order to test the robustness of the isotropic and anisotropic results, two resolution tests were performed. First, a purely isotropic "checkerboard" model was created (Figure 7), consisting of alternating high-velocity and low-velocity regions. For simplicity, no noise is added to the model. After forward modeling to create synthetic group velocity dispersion curves and inverting them using the same approach described in section 4, the checkerboard model was reconstructed. Figure 8 shows these results for 20 s and 30 s periods. An important element of this test is 'leakage' of the 2Ψ anisotropy into the model. As mentioned above, although the input model was purely isotropic, the inversion results exhibit spurious anisotropy directions. The spurious anisotropy is relatively weak, meaning it is approximately <1%, but it does contain potentially misleading artifacts in regions of low path coverage. This can be seen, for example in the northeast corner of both the 20 s and 30 s maps, where there are northwest-southeast trending anisotropy directions, similar to the path directions in this area (Figure 4a). Anisotropy results in areas of low path coverage are therefore disregarded in our interpretations below. In addition, it needs to be stated that this test provides a lower bound on the isotropic bias.

[18] To examine further the robustness of the models and any possible artificial anisotropy in our results, we performed a second resolution test. This test consists of an input model created using isotropic velocities found in our results, with anisotropic directions rotated clockwise by 90 degrees from those of the original results (Figures 9a and 9b). Again, no noise was added to the input model. Reconstruction results (Figures 9c and 9d) for 20 s and 30 s periods recover the input pattern accurately, and in fact appear as a smooth version of the input models; this means that anisotropic directions are generally not biased by path directions or other possible artifacts in the inversion. Quantitative uncertainty in anisotropic directions has been investigated using bootstrap resampling error analysis (see auxiliary material), revealing that, within our main area of interest near the center of Hudson Bay, anisotropy directions have uncertainties within ±30°.[1] In addition, the results are robust with respect to choice of smoothing and damping parameters (see Appendix A).

## 6. Results

[19] Results of the inversion using our preferred parameters are shown in Figure 10. As a rough guideline, the period value in s provides a proxy for the approximate depth of peak sensitivity in km [*Lin et al.*, 2007]. Thus, results for periods of 10–20 s are broadly representative of mid-crustal velocity structure, whereas results for 25–35 s are broadly representative of the lower crust. Red denotes lower isotropic velocities and blue denotes higher isotropic velocities with respect to the regional average for a given period. Through most of the crust there is a relatively low-velocity region near the center of Hudson Bay, as compared with the higher velocities that form a horseshoe shaped region that coincides with the Archean Superior craton (Figure 1b). This regional pattern of isotropic velocity variations is consistent with isotropic tomography results obtained by *Pawlak et al.* [2011], which are based on a different tomographic reconstruction method.

[1]Auxiliary materials are available in the HTML. doi:10.1029/2011JB009066.

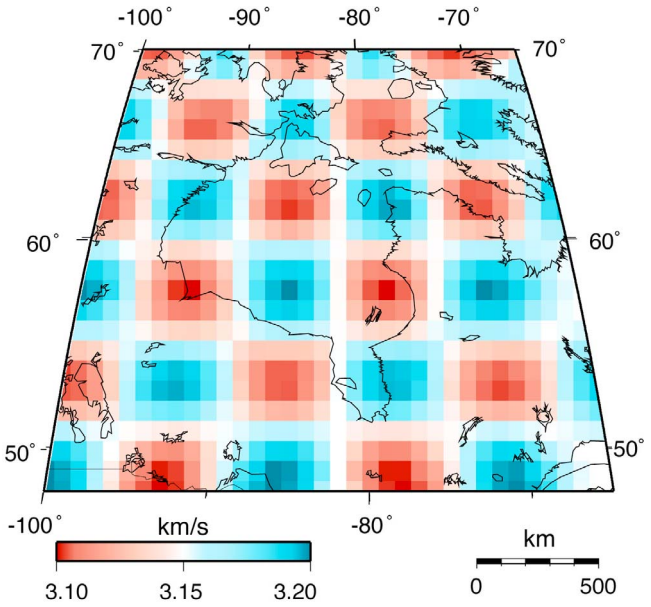


**Figure 7.** Isotropic checkerboard model used for resolution testing.

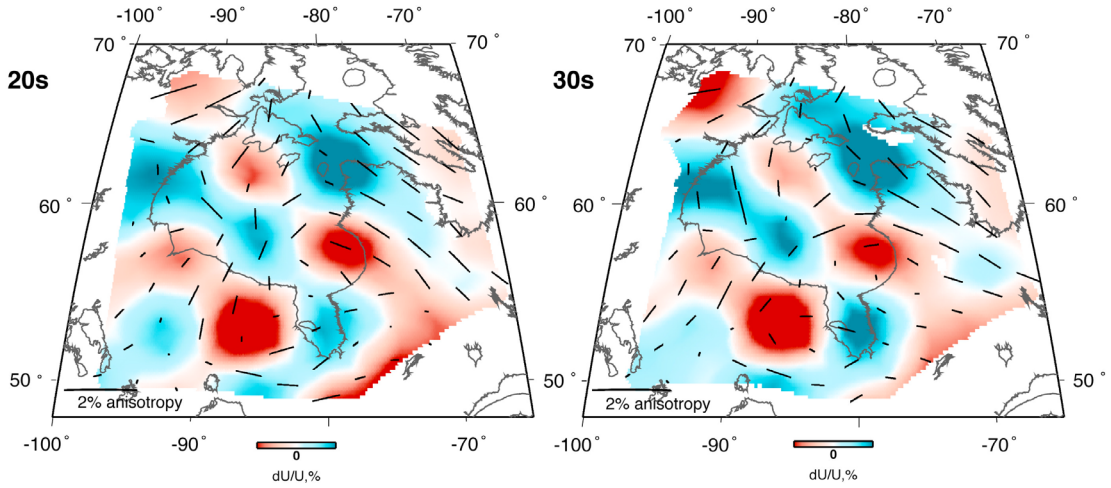


**Figure 8.** Isotropic checkerboard reconstruction results for 20 s and 30 s periods. Isotropic velocities are well resolved, but with some anisotropy 'leaking' through, for example in the northeast corner.

[20] Black bars in Figure 10 show the 2Ψ anisotropy fast directions. A predominant SW-NE fast direction characterizes the mid-crust (10 s–20 s period maps), defining an anisotropic fabric that corresponds well with the surface tectonics of the region. Namely, we observe a large-scale feature that mimics the horseshoe-shaped Superior craton (Figure 1b) ("double indentor" [*Gibb*, 1983; *St Onge et al.*, 2006]), defined as a region of relatively fast isotropic velocities to the south and east of Hudson Bay. Furthermore, within this region the anisotropic fast directions deviate from the dominant SW-NE direction to wrap around in accordance with the 'horseshoe' shaped pattern. This feature is most prominent in the 20 s period map. At periods of 25 s and more, there is a subtle transition in anisotropic fast direction defined by a consistent counterclockwise rotation in fast direction within the central part of Hudson Bay.

## 7. Discussion

[21] Seismological studies of crustal anisotropy typically make use of shear wave splitting [e.g., *Audoine et al.*, 2004] and/or surface-wave tomography methods [e.g., *Gaherty*, 2004]. As noted above, various explanations for observed crustal anisotropy have been suggested. Proposed models for anisotropy include alignment of microcracks [*Crampin et al.*, 1984; *Kaneshima et al.*, 1988], preferred mineral alignment [*Christensen and Mooney*, 1995], fossil anisotropy created during the last tectonic event [*Wüstefeld et al.*, 2010; *Bastow et al.*, 2011], plate motion [*Bokelmann and Wüstefeld*, 2009], stress direction [*Crampin*, 1981] and fabrics defined by geologic structures [*Lin et al.*, 2011]. In this section, we explore some of these models to help determine the origin of the anisotropic fabric in our data.

### 7.1. Crustal Stresses

[22] Seismic anisotropy in the crust could be affected by stress direction as a result of preferred opening of microcracks [*Crampin*, 1981]. Currently, there is sparse data constraining crustal stress directions in Hudson Bay (http://dc-app3-14.gfz-potsdam.de/pub/stress_maps/stress_maps.html). At a large scale, the orientation of maximum compressive stress in the shallow crust can be approximated by absolute plate motion (APM) directions [*Wu*, 1997]. The inferred direction of plate motion in the study area, however depends on the reference frame used [e.g., *Bastow et al.*, 2011], making continent-scale inferences less conclusive. Within the Bay the maximum stress direction is generally NE-SW, although stress-field directions have changed in the last 9000 years due to glacial rebound stress following the last ice age [*Wu*, 1996]. More recent studies based on moment-tensor inversion from local earthquakes have refined the picture of the stress field in northern Hudson Bay [*Steffen et al.*, 2012]. Using data from five earthquakes, *Steffen et al.* [2012] show NNW-SSE directed maximum horizontal stress direction, which is inconsistent with the principal anisotropic fast directions from our study. In view of this mismatch in northern Hudson Bay where the most recent stress information is available, we postulate that patterns of crustal anisotropy throughout Hudson Bay are more likely to reflect frozen crustal deformation that formed during Proterozoic collisional assembly of the lithosphere, rather than a pattern that is strongly influenced by the present-day stress field.

### 7.2. Magnetic Data

[23] Magnetic data have been used in recent years to help interpret observations of seismic anisotropy [*Bokelmann and Wüstefeld*, 2009; *Wüstefeld et al.*, 2010]. Due to the limiting temperature for ferromagnetic behavior and the depth decay for dipole fields ($1/r^3$), magnetic data are well suited for studies of the uppermost lithospheric fabrics [*Wüstefeld et al.*, 2010]. Previous studies [*Bokelmann and Wüstefeld*, 2009] have found a relation between seismic anisotropy in the mantle from shear wave splitting results compared with crustal magnetics. This relation is consistent with vertically coherent deformation, in which the crust and mantle deform as a unit [*Silver and Chan*, 1988]. Since ambient noise studies are generally confined to the crust and uppermost mantle, comparing crustal magnetic features is appropriate.

[24] Magnetic data are available from the Geological Survey of Canada (Figure 11; see also http://www.nrcan.gc.

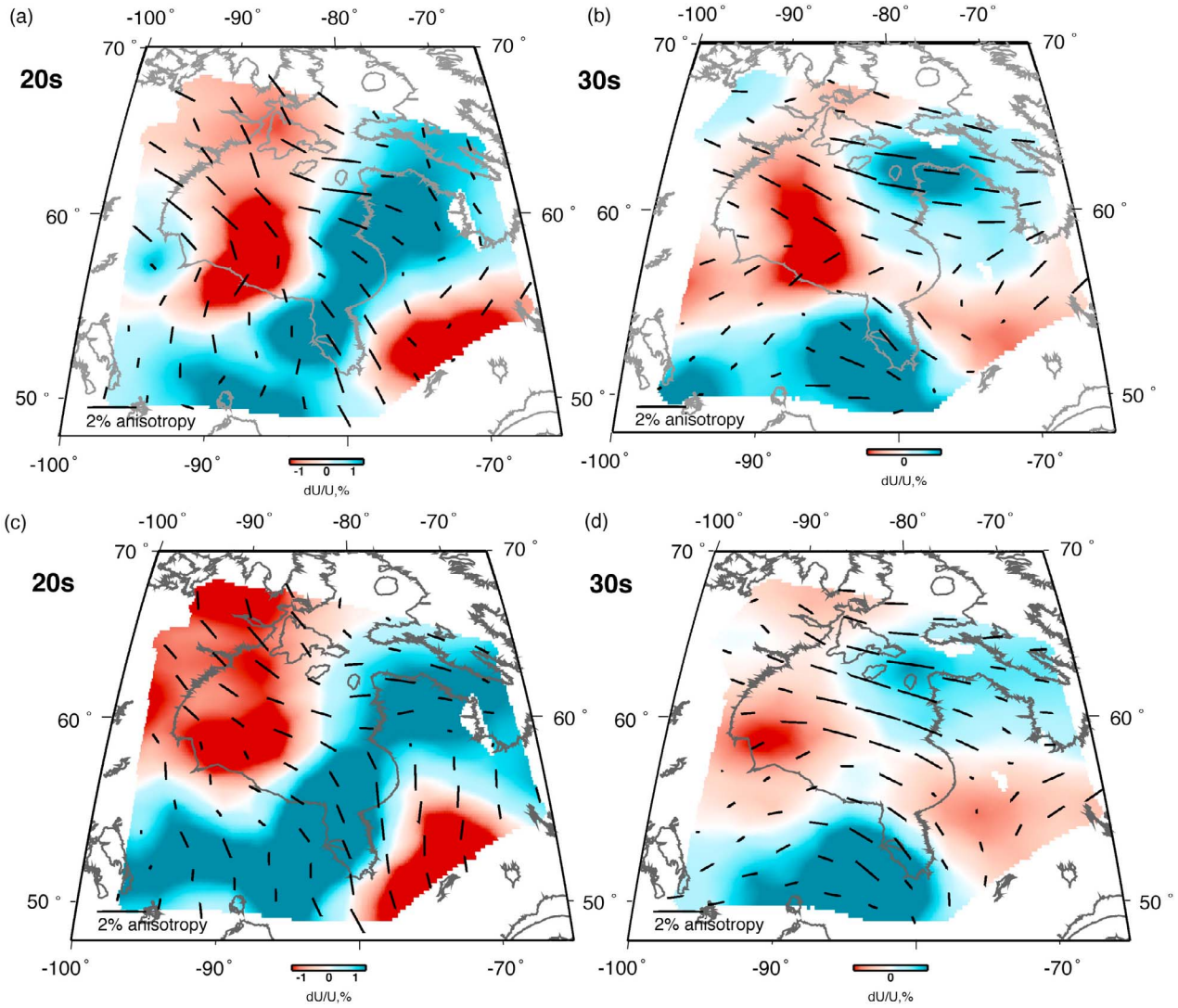


**Figure 9.** Inversion of anisotropy resolution reconstruction results for 20 s and 30 s periods. (a) The input model used for the inversion is the results (Figure 10) with the anisotropic fast direction rotated by 90 degrees at 20 s period; (b) same as Figure 9a for 30 s period. (c, d) Reconstructions of model shown in Figures 9a and 9b. This tests for artifacts in the anisotropic patterns due to the unevenness of the path coverage.

ca/earth-sciences/products-services/geoscience-data-repository/11824). This assemblage of aeromagnetic and marine data is presented on a 400 m grid. Comparing the magnetic data and the 20 s period anisotropic results (Figure 10), there is a very similar pattern in the center of the Bay, showing possible influence of tectonic boundaries. This comparison suggests that the mid-crust has preserved an anisotropic signature similar to that predicted by the magnetic data, indicating that the crust at these depths is likely to have retained an anisotropic structure that dates back to the time of crustal formation in the Precambrian. The 30 s period anisotropy (Figure 10), however, appears to have little correlation to the magnetic data, suggesting that anisotropic fabrics in the lower crust may be characterized by an overprint that is not evident at shallower and deeper levels of the lithosphere. Such a depth dependence of deformation patterns and anisotropy has been documented in regions that are undergoing present-day deformation [e.g., *Endrun et al.*, 2011]. In the case of Hudson Bay, while the anisotropy of the brittle shallow crust may have retained an anisotropic signature since formation, the ductile lower crust/upper mantle anisotropic observations appear to be more sensitive to major mountain building events such as the THO, as is observed in the SKS studies of mantle anisotropy [*Bastow et al.* 2011].

[25] We find that the 20 s period results (Figure 10) are primarily sensitive to the mid crust, whereas the 30 s period results (Figure 10) are sensitive to the lower crust. Knowing this and the decay rate of magnetic data with depth, a similarity between midcrustal patterns of anisotropy and the magnetic anomaly in contrast to the lower crust is physically reasonable. An important feature of all the data sets is a conspicuous change in anisotropy direction on across the suture zone (shown with the red arrows on the magnetic data in Figure 11). This juxtaposition suggests that anisotropic fabrics on either side of the suture formed prior to the termination (ca. 1.86 Ga) of the collision between the Superior

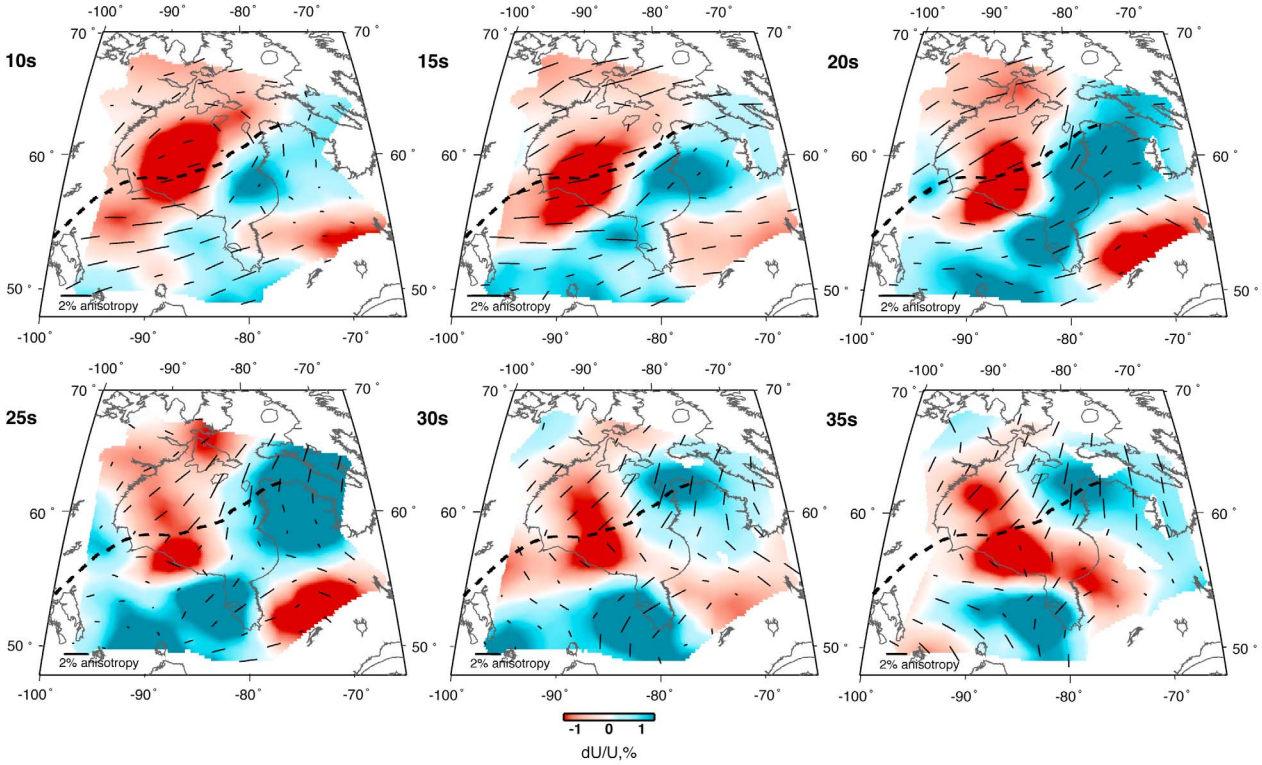


**Figure 10.** Inversion results for periods 10 s, 15 s, 20 s, 25 s, 30 s, and 35 s. Through most of the crust there is a lower velocity region within the center of Hudson Bay, as compared with the higher velocities that form a horseshoe shaped region that coincides with the Archean Superior craton (Figure 1b). Anisotropic fast directions are predominantly SW-NE in the upper crust (10–20 s). There is a significant transition in the pattern at 25 s, carrying through the lower crust (30–35 s). Throughout the crust there is a difference in anisotropic fabric on either side of the inferred THO suture zone shown with a black dashed line (Figure 1b).

craton and the Churchill craton. This observation supports our interpretation that the upper crustal anisotropy patterns preserve a primary tectonic imprint, and also provides a constraint on a minimum age of formation.

### 7.3. Contrasting Crustal Profiles Across the Suture

[26] The THO suture extends across Hudson Bay, separating the Churchill and Superior cratons (Figure 1b) [*Eaton and Darbyshire*, 2010] and it clearly manifests in regional magnetic anomaly data (Figure 11). To explore further how our anisotropic data varies on either side of the suture we show anisotropic dispersion curves (Figure 12) at two representative regions on either side of the suture. Figure 12 shows percent anisotropic amplitude versus period (Figures 12a and 12c) and fast direction azimuth versus period (Figures 12b and 12d) for locations HUB and SUP (Figure 12e). In each region, data from four knot points falling within the chosen region were extracted. The gray lines (Figures 12a and 12c) and gray stars (Figures 12b and 12d) are extracted data and black lines are the averages.

[27] There is a marked contrast in the upper crustal anisotropy (10–20 s). At HUB there is an increase from 0.7 to 1% in amplitude, and an azimuth around 55–60° ± 10°. However, at SUP the amplitude is nearly constant at 0.7%, with an azimuth around 20–40° ± 10°. In the lower crust (30–40 s), there is little contrast between these regions. At HUB the amplitude is ≥1% and azimuth is more constant at around 35° ± 5°. At SUP the amplitude is again more constant at 1% and the azimuth at around 20° ± 5°. Thus, while the upper crust exhibits a discernible change in anisotropy across the suture, the change is less defined in the lower crust.

### 7.4. Tectonic Overprint in the Lower Crust

[28] In the preceding sections, our analysis of regional tectonic fabrics derived from seismic anisotropy indicates depth-dependent behavior within the crust. In particular, at upper- and mid-crustal levels, based on ambient noise recordings with periods of 20 s and less, we observe a good correspondence between fast seismic directions and tectonic fabrics evident from aeromagnetic maps, which are inferred to be representative of tectonometamorphic fabrics. Although robust and spatially coherent, anisotropic fabrics observed at 30 s period (corresponding approximately with lower-crustal depths) are dominated by a generally N-S orientation that crosscuts these tectonic trends in the shallow crust. This inferred depth variation builds on previous work in this area, based on SKS-splitting measurements in an overlapping study region centered immediately north of Hudson Bay [*Bastow et al.*, 2011]. Shear wave splitting in SKS phases yields delay times (delta t) of >1.5 s in much of northern Hudson Bay, where the observations are attributed

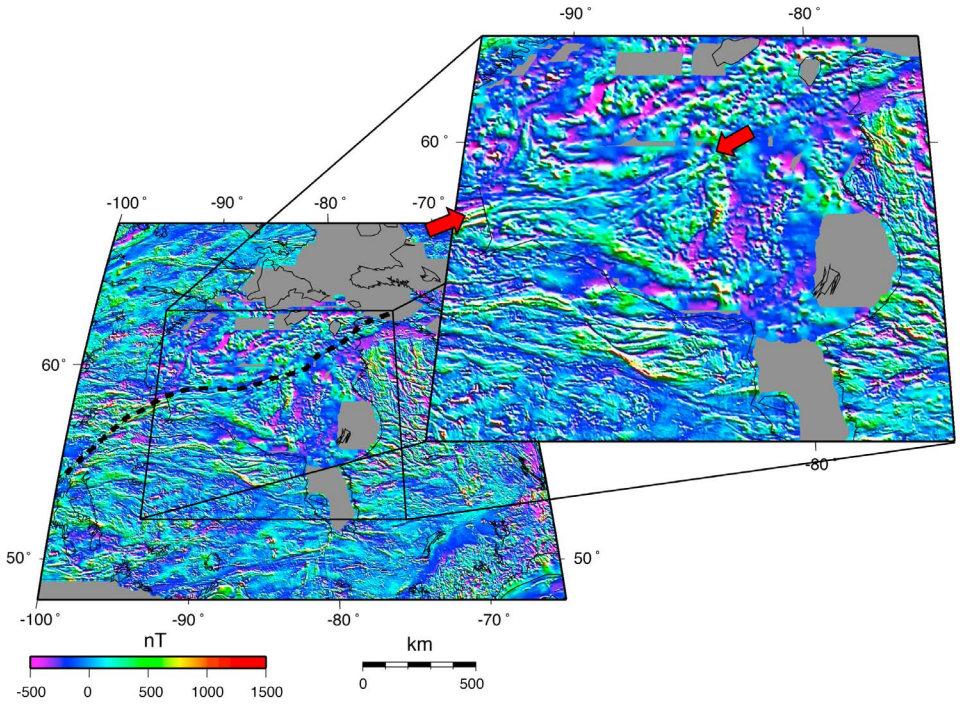


**Figure 11.** Shaded relief image of regional total-field magnetic anomaly data where the black dashed line represents the inferred suture. An enlargement of Hudson Bay highlights the magnetic response along the THO suture zone, indicated by the red arrows.

to plate-scale deformation during the Trans-Hudson Orogen and earlier stages of craton assembly [*Bastow et al.*, 2011] and to deeper asthenospheric fabrics associated with motion of the North American plate [e.g., *Snyder et al.*, 2012]. Toward the SW coast of Hudson Bay, no splitting was observed by *Kay et al.* [1999], who noted moderate-to-large (up to ~2 s) splitting elsewhere. No shear wave splitting studies have been performed using local events in the Hudson Bay region, so it is not clear to what extent the anisotropic fabrics we identify contribute to the SKS observations. However, estimates of the amount of splitting that can be accrued in the crust vary from 0.1 to 0.3 s [*Silver*, 1996] to 0.1–0.5 s [e.g., *Barruol and Mainprice*, 1993] with the implication that crustal anisotropy does not contribute greatly to the SKS observations. In fact, since a vertically propagating S-wave takes ~11 s to travel through a 40 km thick crust, this would, assuming an average 2% anisotropy, only result in 0.2 s of shear wave splitting, which is within the noise of the SKS study [*Silver and Chan*, 1988].

[29] Here, we consider the possibility that observed seismic anisotropy of the lower crust reflects a younger tectonic overprint that is present at neither shallower levels of the crust, nor in the underlying mantle lithosphere. Such a scenario has been described in similar tectonic settings elsewhere. For example, based on geochronology of lower-crustal xenoliths in the southern Superior craton south of Hudson Bay, *Moser and Heaman* [1997] document an episode of zircon growth interpreted to be caused by intrusion of magma into the lower crust during Proterozoic rifting of the craton. Like Hudson Bay, this part of the Superior craton is characterized by SKS splitting results that generally align with regional tectonic trends [e.g., *Frederiksen et al.*, 2007]. Elsewhere, preferential reworking of the lower crust has also been attributed to magmatic underplating within a large igneous province in the Baltic Shield [*Kempton et al.*, 2001], mafic magmatism associated with dike swarms in the Slave craton [*Davis*, 1997], and granulite-facies metamorphism in the North China craton [*Liu et al.*, 2004].

[30] Very low heat flow values documented in nearby regions of the Canadian Shield [e.g., *Rolandone et al.*, 2003] imply that the thermal regime of the entire crust is most likely in the brittle regime. Moreover, modeling of glacial isostatic adjustment [*Wu*, 2002, 2005] treats the entire lithosphere as an elastic plate and models the viscoelastic response within the underlying mantle. We therefore consider that it is very unlikely that the observed lower-crustal anisotropy reflects channel flow in response to GIA within the past 15,000 years. Modern orogenic analogs imply that the channel flow direction follows the gradient from areas of high gravitational potential energy to areas of low potential energy (i.e., roughly perpendicular to topographic relief built up during orogenesis).

[31] The apparent similarity of spatial and temporal characteristics for the Trans-Hudson and Himalayan orogens [*St.-Onge et al.*, 2006] suggests that processes in the lower crust may also be comparable in both cases. A model of gravitationally driven channel flow in the lower crust beneath Tibet is now well established [*Royden et al.*, 1997; *Clark and Royden*, 2000; *Beaumont et al.*, 2001]. The flow propagates through a channel zone in a weak lower crust at a rate driven by temperature, viscosity and horizontal pressure gradient [*Beaumont et al.*, 2001; *Clark et al.*, 2005]. The stresses accumulated are then applied to the elastic upper crust, creating the dynamic topography in Tibet [*Clark et al.*, 2005]. We remark that modeling of Bouguer gravity data within Hudson Bay [*Eaton and Darbyshire*, 2010] and previous

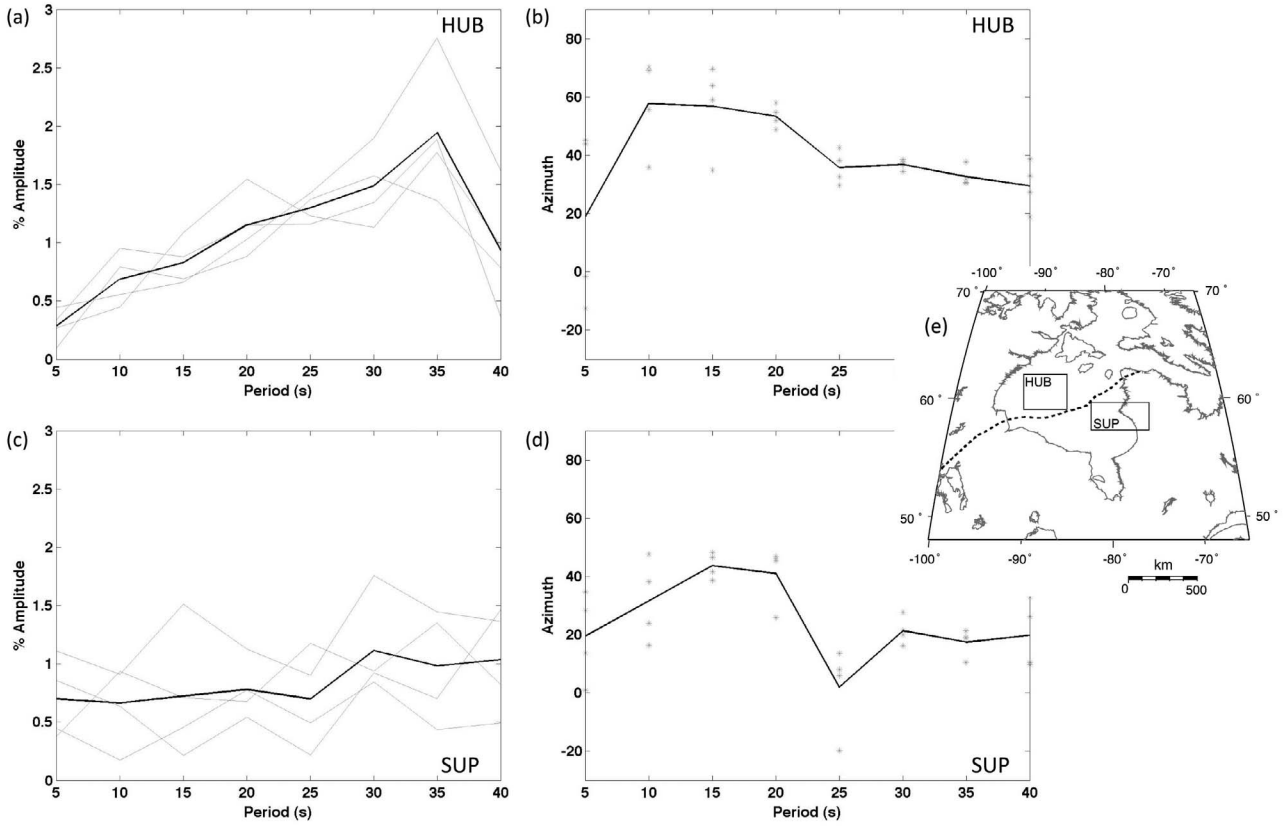


**Figure 12.** Anisotropic dispersion curves on either side of the suture. (a) Grey lines represent percent amplitude perturbation to the regional average for data located at HUB shown in Figure 12e on the north side of the suture. Black line represents the average of the data in from the HUB region. (b) Grey stars show anisotropic fast azimuth distribution for a given period and the black line is the average fast direction azimuth for data in the HUB data. (c) Same as Figure 12a for SUP. (d) Same as Figure 12b for SUP. (e) Location of data for the anisotropic dispersion curves. The black dashed line represents the inferred THO suture zone.

isotropic studies of ambient noise tomography [*Pawlak et al.*, 2011] suggest that lateral variations in density and crustal thickness are preserved in this region. In this context, it is interesting to note that numerical modeling [*Bott*, 1999] indicates that topographic relief and preservation of Moho topography due to local isostasy are both enhanced in the presence of lower-crustal channel flow.

## 8. Conclusions

[32] This study is among the first to use ambient noise data to investigate azimuthal anisotropy. Our inversion method uses smoothing and damping parameters to regularize the solution; due to the significantly increased number of model parameter relative to the isotropic case, considerable attention has been given to investigating whether "leakage" occurs between the isotropic and anisotropic parameters in the inversion. Isotropic velocity patterns found in this study are consistent with results found by *Pawlak et al.* [2011]. Based on analysis of raw data in areas of high path coverage, 4Ψ anisotropy appears to be negligible for the periods of main interest, allowing us to focus on 2Ψ results. This is consistent with certain forms of anisotropy, such as azimuthal anisotropy in hexagonal symmetry systems caused by a single set of aligned cracks or metamorphic fabrics associated with LPO of certain minerals.

[33] The anisotropic fast directions in the mid-crust (20 s period) are consistent with both regional magnetic anomalies and regional tectonic trends. Specifically, our ambient noise inversions and magnetic anomaly maps both reveal a characteristic pattern impacted by a distinctive double-indenter geometry of the Superior craton. Our results also show a significant change in anisotropic direction across an inferred suture beneath Hudson Bay. Previous evidence from SKS-splitting measurements show vertically coherent deformation in the lithosphere; however, in this study the observed anisotropic patterns fade in the lower crust (30 s period). This pattern suggests that a post-orogenic phase of deformation in the lower crust, possibly as a result of channel flow, formed an overprint that was confined to the lower crust.

## Appendix A: Choice of Regularization Parameters

[34] In this section we test smoothing and gradient damping for both isotropic and 2Ψ anisotropic model parameters.

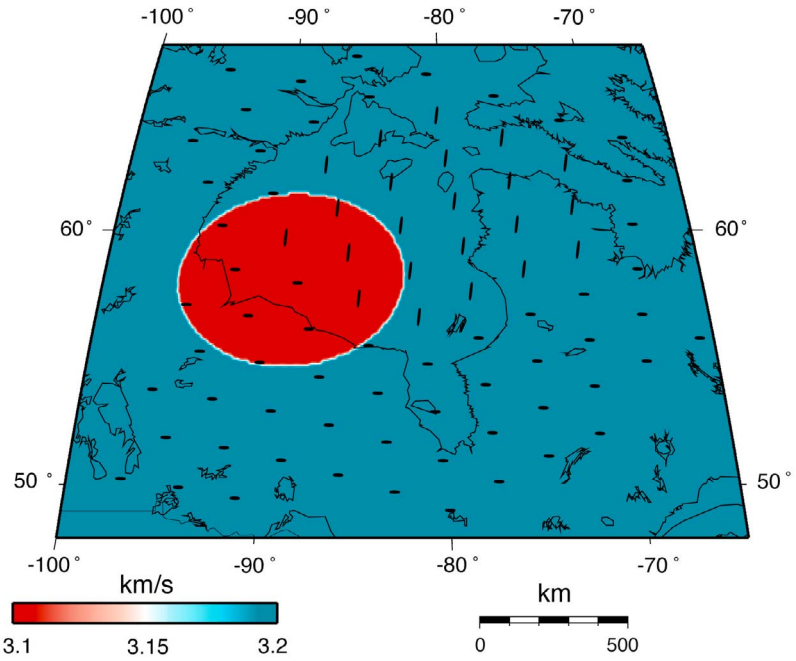


**Figure A1.** Model used for parameter testing, containing an overlapping isotropic anomaly in the SW and an anomalous anisotropic region in the NE part of the study area. Only 2Ψ anisotropy is considered.

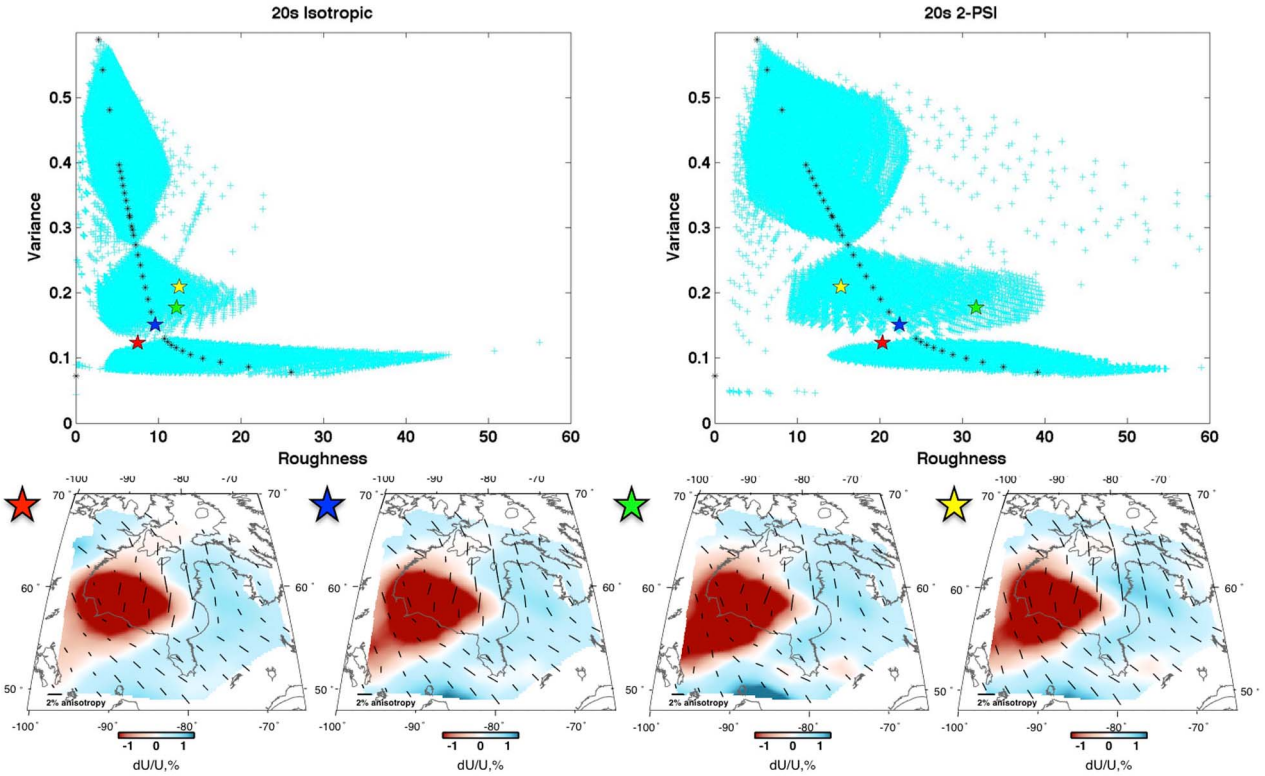


**Figure A2.** Trade-off curves of synthetic data for isotropic and anisotropic variations for various parameter choices. Modeled results are shown for parameter choices indicated with the colored stars.

**Table A1.** Parameter Input and Output Values Corresponding With Stars in Figures A2 and A3[a]

| Chosen Parameters | | | | Resulting Values for Figure A2 | | | |
|---|---|---|---|---|---|---|---|
| Smoothness | | Damping | | Roughness | | | |
| Isotropic | 2Ψ | Isotropic | 2Ψ | Isotropic | 2Ψ | Variance | Star |
| 0.22 | 0.13 | 0.07 | 0.06 | 7.53 | 20.36 | 0.12 | R |
| 0.15 | 0.15 | 0.15 | 0.15 | 9.66 | 22.42 | 0.15 | B |
| 0.10 | 0.10 | 0.25 | 0.30 | 12.19 | 31.71 | 0.17 | G |
| 0.20 | 0.35 | 0.20 | 0.40 | 12.52 | 15.29 | 0.21 | Y |

| Chosen Parameters | | | | Resulting Values for Figure A3 | | | |
|---|---|---|---|---|---|---|---|
| Smoothness | | Damping | | Roughness | | | |
| Isotropic | 2Ψ | Isotropic | 2Ψ | Isotropic | 2Ψ | Variance | Star |
| 0.22 | 0.13 | 0.07 | 0.06 | 8.56 | 27.14 | 0.22 | R |
| 0.15 | 0.15 | 0.15 | 0.15 | 11.50 | 25.51 | 0.25 | B |
| 0.10 | 0.10 | 0.25 | 0.30 | 13.64 | 30.01 | 0.27 | G |
| 0.20 | 0.35 | 0.20 | 0.40 | 13.70 | 14.73 | 0.30 | Y |

[a]A full range of parameters were tested, the above is a subset of what was tested. Abbreviations: R, red; B, blue; G, green; Y, yellow.

The aim of these tests is to evaluate the significance of parameter coupling ("leakage") in which isotropic heterogeneity and anisotropy may trade off with each other in the solution. To this end, our first test model (Figure A1) contains partly overlapping isotropic and anisotropic anomalous regions. The isotropic component has a background velocity of 3.2 km/s with a low-velocity region (3.1 km/s) in the southwest corner. The anisotropic component is confined to 2Ψ anisotropy, with a background fast direction east-west fast direction and an anomalous, strongly anisotropic region with a N-S fast axis, located in the northeast part of the model.

[35] We begin by examining the effects of smoothing and damping parameters to explore their influence on the inversion results. These parameters are analyzed by examining the trade-off between model variance and roughness (Figure A2). The model roughness is the square root of the sum of the squared differences between anomalies at each grid knot and averages over the anomalies at all of its nearest-neighbor knots. The absolute value of the roughness has no physical meaning, but relative changes of the roughness between different tomographic solutions are meaningful. The variance is defined as the data-synthetic variance after the inversion divided by the initial variance. Figure A2 shows trade-offs, one for the isotropic velocity and one for the 2Ψ anisotropy, for 20 s period. Each of the blue points represents a specific combination of 4 parameters, smoothing and damping of the isotropic term and smoothing and damping of the 2-psi term. These results are similar for other periods. The black line represents the case in which all parameters are equal and serves solely as a guide for the trend in the curve.

[36] The overall shape of the curve provides an indication of the behavior of the parameters and furnishes a range of parameter choices. It is clearly desirable to minimize both variance and model roughness simultaneously, since minimizing the variance results in a better fit to the data while

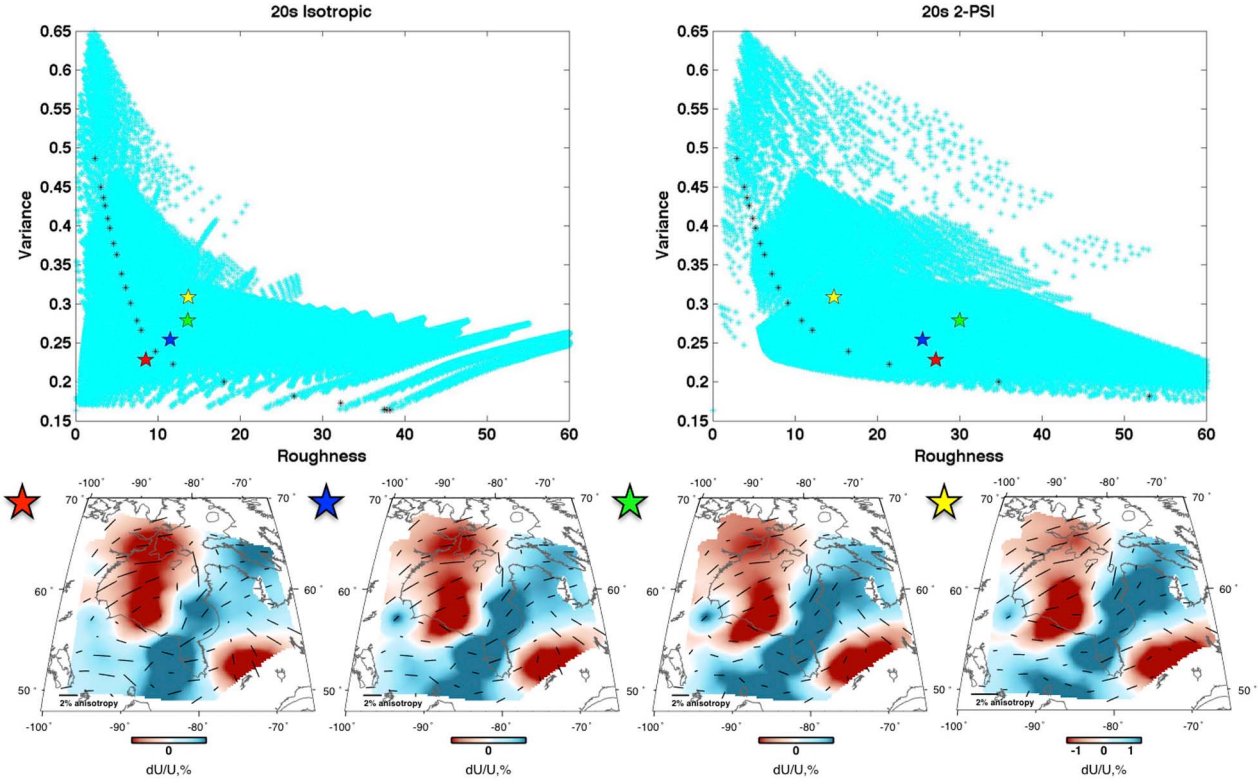


**Figure A3.** Trade-off curves of real data for isotropic and anisotropic variations for various parameter choices. Data results are shown for parameter choices indicated with the colored stars.

minimizing the roughness will reduce artifacts in the result [*Schwarzbach et al.*, 2005]. Generally the 'knee', or the bend that minimizes both the variance and the roughness of the trade-off curve, is thought to indicate the best range of parameters and produce the best results for the data [e.g., *Moorkamp et al.*, 2007].

[37] The solutions for a selection of parameters, chosen arbitrarily such that they fall in the 'knee' zone on both trade-off curves, are shown as stars in Figure A1. The corresponding inversion results are shown below the graphs. The actual values of each of the parameters as well as resulting roughness and variance values are given in Table A1. Each result appears to be consistent with the input model, making it difficult to pick any one as the 'best' parameter. Using the forward model to pick parameters allows us to choose a good range of parameters, but ultimately the parameter selection is highly dependent on the data, so that parameter selection needs to be done using the data as well.

[38] Figure A3 is the same as Figure A2, but it uses the Hudson Bay data set. The stars represent the same parameter choice as in Figure A2. Using the given data set, the parameter values considered in the previous example still fall near the 'knee' zone on both trade-off curves. The isotropic velocity patterns are consistent through all four parameter choices, and are consistent with results found by *Pawlak et al.* [2011]. Anisotropic results generally show the same pattern in all four images. We observe that the red, blue and green star models contain anisotropy directions that form a vortex pattern south of the Bay. This is most likely an artifact arising from the parameter choice, resulting in higher anisotropic roughness. This artifact does not appear in the yellow star model and thus we choose this set of regularization parameters (Table A1) for analysis in this study.

[39] **Acknowledgments.** We are grateful to Honn Kao, from the Pacific Geoscience Center in Sydney, British Columbia, for providing us with initial data and assistance with data processing. We thank other members of the HuBLE working group for stimulating discussions and the CREWES project at the University of Calgary for their support. Thank you to C-NGO and the First Nation communities around Hudson Bay for allowing seismometer deployments. GMT [*Wessel and Smith*, 1995] and dispersion code written by R. Herrmann was used in the preparation of some figures. Natural Environment Research Council (NERC) stations were supported by grant NE/F007337/1. This study was supported by NSERC through a Discovery grant to D.W.E. I.B. was funded by the Leverhulme Trust.

## References

Audoine, E. L., M. K. Savage, and K. R. Gledhill (2004), Anisotropic structure under a back-arc spreading region, the Taupo Volcanic Zone, New Zealand, *J. Geophys. Res.*, *109*, B11305, doi:10.1029/2003JB002932.

Barruol, G., and D. Mainprice (1993), 3-D seismic velocities calculated from lattice-preferred orientation and reflectivity of a lower crustal section: Examples of the Val Sesia section (Ivrea zone, northern Italy), *Geophys. J. Int.*, *115*, 1169–1188, doi:10.1111/j.1365-246X.1993.tb01519.x.

Bastow, I. D., D. Thompson, J. Wookey, J. M. Kendall, G. Helffrich, D. Snyder, D. W. Eaton, and F. A. Darbyshire (2011), Precambrian plate tectonics: Seismic evidence from northern Hudson Bay, Canada, *Geology*, *39*, 91–94, doi:10.1130/G31396.1.

Beaumont, C., R. A. Jamieson, M. H. Nguyen, and B. Lee (2001), Himalayan tectonics explained be extrusion of a low-viscosity crustal channel coupled to focused surface denudation, *Nature*, *414*, 738–742, doi:10.1038/414738a.

Bensen, G. D., M. H. Ritzwoller, M. P. Barmin, A. L. Levshin, F. C. Lin, M. P. Moschetti, N. M. Shapiro, and Y. Yang (2007), Processing seismic ambient noise data to obtain reliable broad-band surface wave dispersion measurements, *Geophys. J. Int.*, *169*, 1239–1260, doi:10.1111/j.1365-246X.2007.03374.x.

Bickford, M. E., K. D. Collerson, J. F. Lewry, W. R. Van Schmus, and J. R. Chiarenzelli (1990), Proterozoic collisional tectonism in the Trans-Hudson Orogen, Saskatchewan, *Geology*, *18*, 14–18, doi:10.1130/0091-7613(1990)018<0014:PCTITT>2.3.CO;2.

Bokelmann, G. H. R., and A. Wüstefeld (2009), Comparing crustal and mantle fabric from the North American craton using magnetics and seismic anisotropy, *Earth Planet. Sci. Lett.*, *277*(3–4), 355–364, doi:10.1016/j.epsl.2008.10.032.

Bott, M. H. P. (1999), Modeling local crustal isostasy caused by ductile flow in the lower crust, *J. Geophys. Res.*, *104*, 20,349–20,359, doi:10.1029/1999JB900182.

Brocher, T. M., and N. I. Christensen (1990), Seismic anisotropy due to preferred mineral orientation observed in shallow crustal rocks in southern Alaska, *Geology*, *18*, 737–740, doi:10.1130/0091-7613(1990)018<0737:SADTPM>2.3.CO;2.

Burden, E. T., and A. B. Langille (1990), Stratigraphy and sedimentology of Cretaceous and Paleocene strata in half-grabens on the southeast coast of Baffin Island, *Bull. Can. Pet. Geol.*, *38*, 185–196.

Christensen, N. I., and W. D. Mooney (1995), Seismic velocity structure and composition of the continental crust: A global view, *J. Geophys. Res.*, *100*, 9761–9788, doi:10.1029/95JB00259.

Clark, M. K., and L. H. Royden (2000), Topographic ooze: Building the eastern margin of Tibet by lower crustal flow, *Geology*, *28*, 703–706, doi:10.1130/0091-7613(2000)28<703:TOBTEM>2.0.CO;2.

Clark, M. K., J. W. M. Bush, and L. H. Royden (2005), Dynamic topography produced by lower crustal flow against rheological strength heterogeneities bordering the Tibetan Plateau, *Geophys. J. Int.*, *162*, 575–590, doi:10.1111/j.1365-246X.2005.02580.x.

Corrigan, D., Z. Hajnal, B. Németh, and S. B. Lucas (2005), Tectonic framework of a paleoprotoerozoic arc-continent to continent-continent collisional zone, Trans-Hudson Orogen, from geological and seismic reflection studies, *Can. J. Earth Sci.*, *42*, 421–434, doi:10.1139/e05-025.

Crampin, S. (1981), A review of wave motion in anisotropic and cracked elastic-media, *Wave Motion*, *3*, 343–391, doi:10.1016/0165-2125(81)90026-3.

Crampin, S. (1987), Geological and industrial implications of extensive-dilatancy anisotropy, *Nature*, *328*, 491–496, doi:10.1038/328491a0.

Crampin, S. (1994), The fracture criticality of crustal rocks, *Geophys. J. Int.*, *118*, 428–438, doi:10.1111/j.1365-246X.1994.tb03974.x.

Crampin, S., E. M. Chesnokov, and R. G. Hipkin (1984), Seismic anisotropy—The state of the art: II, *Geophys. J. R. Astron., Soc.*, *76*, 1–16.

Curtis, A., P. Gerstoft, H. Sato, R. Snieder, and K. Wapenaar (2006), Seismic interferometry—Turning noise into signal, *Leading Edge*, *25*, 1082–1092.

Darbyshire, F. A., and D. W. Eaton (2010), The lithospheric root beneath Hudson Bay, Canada from Rayleigh-wave dispersion: No clear seismological distinction between Archean and Proterozoic mantle, *Lithos*, *120*, 144–159, doi:10.1016/j.lithos.2010.04.010.

Darbyshire, F. A., and S. Lebedev (2009), Rayleigh wave phase-velocity heterogeneity and multilayered azimuthal anisotropy of the Superior Craton, Ontario, *Geophys. J. Int.*, *176*, 215–234, doi:10.1111/j.1365-246X.2008.03982.x.

Davis, W. J. (1997), U-Pb zircon and rutile ages from granulite xenoliths in the Slave province: Evidence for mafic magmatism in the lower crust coincident with Proterozoic dike swarms, *Geology*, *25*, 343–346, doi:10.1130/0091-7613(1997)025<0343:UPZARA>2.3.CO;2.

Deschamps, F., S. Lebedev, T. Meier, and J. Trampert (2008), Azimuthal anisotropy of Rayleigh-wave phase velocities in the east-central United States, *Geophys. J. Int.*, *173*, 827–843, doi:10.1111/j.1365-246X.2008.03751.x.

Drulea, M., I. R. Peter, and S. Nedevschi (2010), Optical flow: A combined local-global approach using L1 norm, paper presented at International Conference on Intelligent Computer Communication and Processing, Inst. of Electr. and Electr. Eng., Cluj-Napoca, Romania.

Eaton, D. W., and F. A. Darbyshire (2010), Lithospheric architecture and tectonic evolution of the Hudson Bay region, *Tectonophysics*, *480*, 1–22, doi:10.1016/j.tecto.2009.09.006.

Endrun, B., S. Lebedev, T. Meier, C. Tirel, and W. Friederich (2011), Complex layered deformation within the Aegean crust and mantle revealed by seismic anisotropy, *Nat. Geosci.*, *4*, 203–207, doi:10.1038/ngeo1065.

Frederiksen, A. W., S.-K. Miong, F. A. Darbyshire, D. W. Eaton, S. Rondenay, and S. Sol (2007), Lithospheris variations across the Superior Province, Ontario, Canada: Evidence from tomography and shear wave splitting, *J. Geophys. Res.*, *112*, B07318, doi:10.1029/2006JB004861.

Fry, B., F. Deschamps, E. Kissling, L. Stehly, and D. Giardini (2010), Layered azimuthal anisotropy of Rayleigh wave phase velocities in the European Alpine lithosphere inferred from ambient noise, *Earth Planet. Sci. Lett.*, *297*, 95–102, doi:10.1016/j.epsl.2010.06.008.

Gaherty, J. B. (2004), A surface wave analysis of seismic anisotropy beneath eastern North America, *Geophys. J. Int.*, *158*, 1053–1066, doi:10.1111/j.1365-246X.2004.02371.x.

Gallego, A., M. P. Panning, R. M. Russo, V. I. Mocanu, R. E. Murdie, and J. C. VanDecar (2011), Azimuthal anisotropy in the Chile Ridge subduction region retrieved from ambient noise, *Lithos*, *3*, 393–400, doi:10.1130/L139.1.

Gay, S. P. (1973), *Pervasive Orthogonal Fracturing in the Earth's Continental Crust*, Am. Stereo Map Co., Salt Lake City, Utah.

Gibb, R. A. (1983), Model for suturing of Superior and Churchill plates: An example of double-indentation tectonics, *Geology*, *11*, 413–417, doi:10.1130/0091-7613(1983)11<413:MFSOSA>2.0.CO;2.

Hajnal, Z., J. F. Lewry, D. J. White, K. Ashton, R. M. Clowes, M. Stauffer, I. Gyorfi, and E. Takacs (2005), The Sask Craton and Hearne Province margin: Seismic reflection studies in the western Trans_Hudson Orogen, *Can. J. Earth Sci.*, *42*, 403–419, doi:10.1139/e05-026.

Hoffman, P. F. (1990), Subdivision of the Churchill Province and extent of the Trans-Hudson Orogen, in *The Early Proterozioc Trans-Hudson Orogen of North America*, edited by J. F. Lewry and M. R. Stauffer, *Spec. Pap. Geol. Assoc. Can.*, *37*, 15–39.

Kaneshima, S., M. Ando, and S. Kimura (1988), Evidence from shear-wave splitting for restriction of seismic anisotropy to the upper crust, *Nature*, *335*, 627–629, doi:10.1038/335627a0.

Kay, I., S. Sol, J.-M. Kendall, C. Thomson, D. White, I. Asudeh, B. Roberts, and D. Francis (1999), Shear wave splitting observation in the Archean Craton of Western Superior, *Geophys. Res. Lett.*, *26*, 2669–2672, doi:10.1029/1999GL010493.

Kempton, P. D., H. Downes, L. A. Neymark, J. A. Wartho, R. E. Zartman, and E. V. Sharkov (2001), Garnet granulite xenoliths from northern Baltic Shield—The underplated lower crust of a palaeoproterozoic large igneous province?, *J. Petrol.*, *42*, 731–763, doi:10.1093/petrology/42.4.731.

Lebedev, S., and R. D. van der Hilst (2008), Global upper-mantle tomography with the automated multimode inversion of surface and S wave forms, *Geophys. J. Int.*, *173*, 505–518, doi:10.1111/j.1365-246X.2008.03721.x.

Lee, H. A. (1968), Quaternary geology, in *Science, History and Hudson Bay*, vol. 1–2, edited by C. S. Beals, pp. 503–543, Dep. of Energy Min. and Resour., Ottawa, Ont., Canada.

Lin, F. C., M. H. Ritzwoller, J. Townend, M. Savage, and S. Bannister (2007), Ambient noise Rayleigh wave tomography of New Zealand, *Geophys. J. Int.*, *170*, 649–666, doi:10.1111/j.1365-246X.2007.03414.x.

Lin, F. C., M. H. Ritzwoller, Y. Yang, M. P. Moschetti, and M. J. Fouch (2011), Complex and variable crustal and uppermost mantle seismic anisotropy in the western United States, *Nat. Geosci.*, *4*, 55–61, doi:10.1038/ngeo1036.

Liu, Y., S. Gao, H. Yuan, L. Zhou, X. Liu, X. Wang, Z. Hu, and L. Wang (2004), U-Pb zircon ages and Nd, Sr, and Pb isotopes of lower crustal xenoliths from North China Craton: Insights on evolution of lower continental crust, *Chem. Geol.*, *211*, 87–109, doi:10.1016/j.chemgeo.2004.06.023.

Mahan, K. (2006), Retrograde mica in deep crustal granulites: Implications for crustal seismic anisotropy, *Geophys. Res. Lett.*, *33*, L24301, doi:10.1029/2006GL028130.

Mandeville, C. W. (2010), Sulfur: A ubiquitous and useful tracer in Earth and planetary sciences, *Elements*, *6*, 75–80, doi:10.2113/gselements.6.2.75.

Meltzer, A., and N. Christensen (2001), Nanga Parbat crustal anisotropy: Implications for interpretation of crustal velocity structure and shear-wave splitting, *Geophys. Res. Lett.*, *28*, 2129–2132, doi:10.1029/2000GL012262.

Moorkamp, M., A. G. Jones, and D. W. Eaton (2007), Joint inversion of teleseismic receiver functions and magnetotelluric data using a genetic algorithm: Are seismic velocities and electrical conductivities compatible?, *Geophys. Res. Lett.*, *34*, L16311, doi:10.1029/2007GL030519.

Moschetti, M. P., M. H. Ritzwoller, and N. M. Shapiro (2007), Surface wave tomography of the western United States from ambient seismic noise: Rayleigh wave group velocity maps, *Geochem. Geophys. Geosyst.*, *8*, Q08010, doi:10.1029/2007GC001655.

Moschetti, M. P., M. H. Ritzwoller, and F. C. Lin (2010), Seismic evidence for widespread crustal deformation caused be extension in the western USA, *Nature*, *464*, 885–889, doi:10.1038/nature08951.

Moser, D. E., and L. M. Heaman (1997), Proterozoic zircon growth in Archean lower crustal xenoliths, southern Superior craton—A consequence of Matachewan ocean opening, *Contrib. Mineral. Petrol.*, *128*, 164–175, doi:10.1007/s004100050301.

Paige, C. C., and M. A. Saunders (1982), LSQR: An algorithm for sparse linear equations and sparse least squares, *Assoc. Comput. Mach. Trans. Math. Software*, *8*, 43–71, doi:10.1145/355984.355989.

Paulssen, H. (2004), Crustal anisotropy in southern California from local earthquake data, *Geophys. Res. Lett.*, *31*, L01601, doi:10.1029/2003GL018654.

Pawlak, A. P., D. W. Eaton, I. D. Bastow, J. M. Kendall, G. Helffrich, J. Wookey, and D. Snyder (2011), Crustal structure beneath Hudson Bay from ambient noise tomography: Implications for basin formation, *Geophys. J. Int.*, *184*, 65–82, doi:10.1111/j.1365-246X.2010.04828.x.

Rolandone, F., J. C. Mareschal, C. Jaupart, C. Gosselin, G. Bienfait, and R. Lapointe (2003), Heat flow in the western Superior Province of the Canadian shield, *Geophys. Res. Lett.*, *30*(12), 1637, doi:10.1029/2003GL017386.

Royden, L. H., B. C. Burchfiel, R. W. King, E. Wang, Z. Chen, F. Shen, and Y. Liu (1997), Surface deformation and lower crustal flow in eastern Tibet, *Science*, *276*, 788–790, doi:10.1126/science.276.5313.788.

Schwarzbach, C., R. U. Börner, and K. Spitzer (2005), Two-dimensional inversion of direct current resistivity data using a parallel, multi-objective genetic algorithm, *Geophys. J. Int.*, *162*, 685–695, doi:10.1111/j.1365-246X.2005.02702.x.

Shapiro, N. M., M. H. Ritzwoller, P. Molar, and V. Levin (2004), Thinning and flow of Tibetan crust constrained by seismic anisotropy, *Science*, *305*, 233–236, doi:10.1126/science.1098276.

Shapiro, N. M., M. Campillo, L. Stehly, and M. H. Ritzwoller (2005), High resolution surface wave tomography from ambient seismic noise, *Science*, *307*, 1615–1618, doi:10.1126/science.1108339.

Silver, P. G. (1996), Seismic anisotropy beneath the continents: Probing the depths of geology, *Annu. Rev. Earth Planet. Sci.*, *24*, 385–432, doi:10.1146/annurev.earth.24.1.385.

Silver, P. G., and W. W. Chan (1988), Implications for crustal structure and evolution from seismic anisotropy, *Nature*, *335*, 34–39, doi:10.1038/335034a0.

Smith, M. L., and F. A. Dahlen (1973), The azimuthal dependence of Love and Rayleigh wave propagation in a slightly anisotropic medium, *J. Geophys. Res.*, *78*, 3321–3333, doi:10.1029/JB078i017p03321.

Smith, D. B., M. H. Ritzwoller, and N. M. Shapiro (2004), Stratification of anisotropy in the Pacific upper mantle, *J. Geophys. Res.*, *109*, B11309, doi:10.1029/2004JB003200.

Snyder, D. B., and R. G. Berman, J. M. Kendall, and M. Sanborn-Barrie (2012), Seismic anisotropy and mantle structure of the Rae Craton, Central Canada, from joint interpretation of SKS splitting and receiver functions, *Precambrian Res.*, doi:10.1016/j.precamres.2012.03.003, in press.

St.-Onge, M. R., M. P. Searle, and N. Wodicka (2006), Trans-Hudson Orogen of North America and Himalaya-Karakoram-Tibetan Orogen of Asia: Structural and thermal characteristics of the lower and upper plates, *Tectonics*, *25*, TC4006, doi:10.1029/2005TC001907.

Steffen, R., D. W. Eaton, and P. Wu (2012), Moment tensors, state of stress and their relation to postglacial rebound in northeastern Canada, *Geophys. J. Int.*, *189*(3), 1741–1752, doi:10.1111/j.1365-246X.2012.05452.x.

Symons, D. T. A., and M. J. Harris (2005), Accretion history of the Trans-Hudson Orogen in Manitoba and Saskatchewan from paleomagnetism, *Can. J. Earth Sci.*, *42*, 723–740, doi:10.1139/e04-090.

Thompson, D. A., I. D. Bastow, G. Helffrich, J. M. Kendall, J. Wookey, D. Snyder, and D. W. Eaton (2010), Precambrian crustal evolution of the Canadian Shield: Constraints from receiver function analysis, *Earth Planet. Sci. Lett.*, *297*, 655–666, doi:10.1016/j.epsl.2010.07.021.

Thompson, D. A., G. Helffrich, I. D. Bastow, J. Wookey, J.-M. Kendall, D. Eaton, and D. Snyder (2011), Implications of a simple mantle transition zone beneath cratonic North America, *Earth Planet. Sci. Lett.*, *312*, 28–36, doi:10.1016/j.epsl.2011.09.037.

Wang, Z., and F. A. Dahlen (1995), Spherical-spline parameterization of 3-dimensional earth models, *Geophys. Res. Lett.*, *22*, 3099–3102, doi:10.1029/95GL03080.

Wessel, P., and W. H. F. Smith (1995), New Version of the Generic Mapping Tools Released, *Eos Trans. AGU*, *76*, 329, doi:10.1029/95EO00198.

Winterstein, D. F. (1990), Velocity anisotropy terminology for geophysicists, *Geophysics*, *55*, 1070–1088, doi:10.1190/1.1442919.

Winterstein, D. (1992), How shear-wave properties relate to rock fractures: Simple cases, *Leading Edge*, *11*(9), 21–28, doi:10.1190/1.1436900.

Wu, P. (1996), Changes in orientation of near-surface stress field as constraints to mantle viscosity and horizontal stress differences in Eastern Canada, *Geophys. Res. Lett.*, *23*, 2263–2266, doi:10.1029/96GL02149.

Wu, P. (1997), Effect of viscosity structure on fault potential and stress orientations in eastern Canada, *Geophys. J. Int.*, *130*, 365–382, doi:10.1111/j.1365-246X.1997.tb05653.x.

Wu, P. (2002), Effects of mantle flow law stress exponent on postglacial induced surface motion and gravity in Laurentia, *Geophys. J. Int.*, *148*, 676–686, doi:10.1046/j.1365-246X.2002.01620.x.

Wu, P. (2005), Effects of lateral variations in lithospheric thickness and mantle viscosity on glacially induced surface motion in Laurentia, *Earth Planet. Sci. Lett.*, *235*, 549–563, doi:10.1016/j.epsl.2005.04.038.

Wüstefeld, A., G. Bokelmann, and G. Barruol (2010), Evidence for ancient lithospheric deformation in the Eat European Craton based on mantle seismic anisotropy and crustal magnetics, *Tectonophysics*, *481*, 16–28, doi:10.1016/j.tecto.2009.01.010.

Yang, Y., M. H. Ritzwoller, A. L. Levshin, and N. M. Shapiro (2007), Ambient noise Rayleigh wave tomography across Europe, *Geophys. J. Int.*, *168*, 259–274, doi:10.1111/j.1365-246X.2006.03203.x.

Yao, H. J., and R. D. van der Hilst (2009), Analysis of ambient noise energy distribution and phase velocity bias in ambient noise tomography, with application to SE Tibet, *Geophys. J. Int.*, *179*, 1113–1132, doi:10.1111/j.1365-246X.2009.04329.x.

Yao, H., R. D. van der Hilst, and M. V. de Hoop (2006), Surface-wave tomography in SE Tibet from ambient seismic noise and two-station analysis: I.- Phase velocity maps, *Geophys. J. Int.*, *166*, 732–744, doi:10.1111/j.1365-246X.2006.03028.x.

Zhang, S., and S.-I. Karato (1995), Lattice preferred orientation of olivine aggregates deformed in simple shear, *Nature*, *375*, 774–777, doi:10.1038/375774a0.